# Glasses and Glass Ceramics

## Current state of research in the synthesis, modification, and characterization
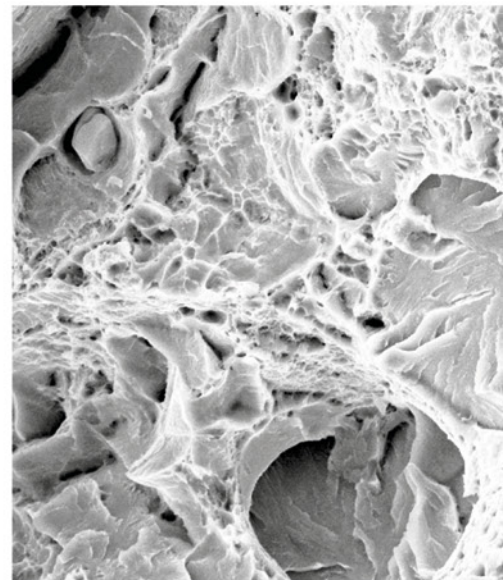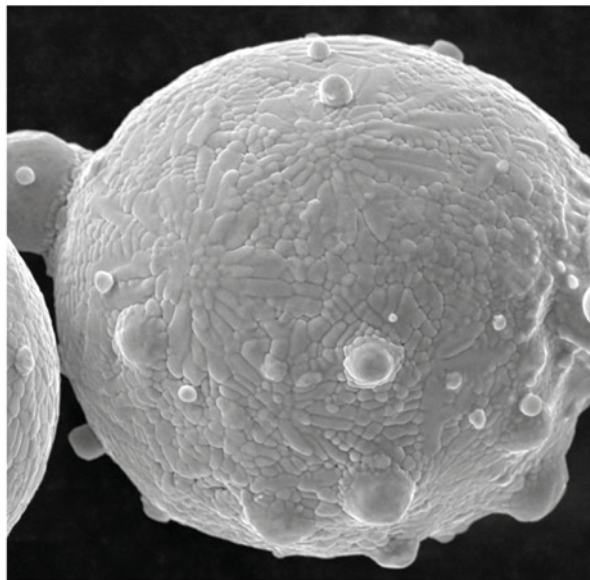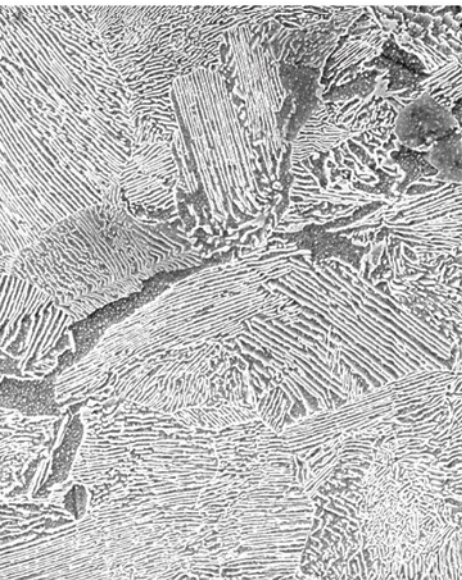
WILEY

**POLYTECH**
Peter the Great
St. Petersburg Polytechnic
University

# Liquid-Metal Synthesized Ultrathin SnS Layers for High-Performance Broadband Photodetectors

Vaishnavi Krishnamurthi, Hareem Khan, Taimur Ahmed,* Ali Zavabeti, Sherif Abdulkader Tawfik, Shubhendra Kumar Jain, Michelle J. S. Spencer, Sivacarendran Balendhran, Kenneth B Crozier, Ziyuan Li, Lan Fu, Md Mohiuddin, Mei Xian Low, Babar Shabbir, Andreas Boes, Arnan Mitchell, Christopher F. McConville, Yongxiang Li, Kourosh Kalantar-Zadeh, Nasir Mahmood,* and Sumeet Walia*

Atomically thin materials face an ongoing challenge of scalability, hampering practical deployment despite their fascinating properties. Tin monosulfide (SnS), a low-cost, naturally abundant layered material with a tunable bandgap, displays properties of superior carrier mobility and large absorption coefficient at atomic thicknesses, making it attractive for electronics and optoelectronics. However, the lack of successful synthesis techniques to prepare large-area and stoichiometric atomically thin SnS layers (mainly due to the strong interlayer interactions) has prevented exploration of these properties for versatile applications. Here, SnS layers are printed with thicknesses varying from a single unit cell (0.8 nm) to multiple stacked unit cells (≈1.8 nm) synthesized from metallic liquid tin, with lateral dimensions on the millimeter scale. It is reveal that these large-area SnS layers exhibit a broadband spectral response ranging from deep-ultraviolet (UV) to near-infrared (NIR) wavelengths (i.e., 280–850 nm) with fast photodetection capabilities. For single-unit-cell-thick layered SnS, the photodetectors show upto three orders of magnitude higher responsivity (927 A W$^{-1}$) than commercial photodetectors at a room-temperature operating wavelength of 660 nm. This study opens a new pathway to synthesize reproduceable nanosheets of large lateral sizes for broadband, high-performance photodetectors. It also provides important technological implications for scalable applications in integrated optoelectronic circuits, sensing, and biomedical imaging.

2D materials have been a major focus for a plethora of scientific discoveries, ever since the isolation of graphene from its bulk crystal. However, the tremendous potential of post transition metal monochalcogenides[1–3] such as the Group IV monochalcogenides (MX, M = Sn, Ge, Pb, etc. and X = S, Se) remains relatively untapped.[4] Theoretical studies of these materials have revealed peculiar electronic and optoelectronic properties at their quantum limit but are yet to receive an experimental thrust[5] primarily due to the inability to obtain large aspect ratios. Semiconducting SnS is a representative member of the family of post transition metal monochalcogenides that exist in an orthorhombic layered structure.[6,7] The buckled structure of SnS is held together with weak van der Waals (vdW) forces between the layers exhibiting structural anisotropy, a feature very similar to the isoelectronic structure of black phosphorus (BP)[1,7] (See Note 1, Supporting Information). As a p-type semiconductor, SnS has both indirect and

V. Krishnamurthi, H. Khan, Dr. T. Ahmed, Dr. A. Zavabeti, S. K. Jain,
Dr. M. Mohiuddin, M. X. Low, Dr. A. Boes, Prof. A. Mitchell, Prof. Y. Li,
Dr. N. Mahmood, Prof. S. Walia
School of Engineering
RMIT University
124 La Trobe Street, Melbourne, Victoria 3001, Australia
E-mail: taimur.ahmed@rmit.edu.au; nasir.mahmood@rmit.edu.au;
sumeet.walia@rmit.edu.au
Dr. T. Ahmed, S. K. Jain, M. X. Low, Prof. S. Walia
Functional Materials and Microsystems Research Group and the
Micro Nano Research Facility
RMIT University
124 La Trobe Street, Melbourne, Victoria 3001, Australia

The ORCID identification number(s) for the author(s) of this article
can be found under https://doi.org/10.1002/adma.202004247.

[+]Present address: Institute for Frontier Materials, Deakin University,
Geelong, Victoria 3220, Australia

Dr. A. Zavabeti
Department of Chemical Engineering
The University of Melbourne
Melbourne, Victoria 3010, Australia
Dr. S. A. Tawfik, Prof. M. J. S. Spencer, Prof. C. F. McConville[+]
School of Science
RMIT University
Melbourne, Victoria 3001, Australia
S. K. Jain
Sensor Devices and Metrology Group
CSIR—National Physical Laboratory (CSIR-NPL)
Dr K. S. Krishnan Road, New Delhi 110012, India
S. K. Jain
Academy of Scientific & Innovative Research
(AcSIR)
CSIR-HRDC Campus, Ghaziabad, Uttar Pradesh 201002, India

**ADVANCED
SCIENCE NEWS**
www.advancedsciencenews.com

**ADVANCED
MATERIALS**
www.advmat.de

direct-bandgap energies reported in the range ≈1.0–1.3 eV and ≈1.3–1.5 eV, respectively.[7] The bandgap tunability allows it to exhibit a combination of desirable electronic and optoelectronic properties[8–10] that include large absorption coefficient[11] across a wide wavelength range, tunable electrical conductivity,[12] and high carrier mobility.[6] This renders SnS a suitable candidate for multidisciplinary applications such as photodetectors,[13] photovoltaic cells,[14] field-effect transistors,[15] and spin-valley lasers.[16] However, conventional growth and synthesis strategies such as chemical vapor deposition and physical vapor deposition have failed to attain good quality atomically-thin SnS due to the formation of uncontrolled grain orientations, defects, and impurities.[17–19] Strong inter layer interactions resulting from lone pair electrons associated with each S atom is a prominent reason for the inability to isolate ultrathin layers of SnS[6] using established mechanical cleaving processes. These interactions are stronger than the vdW forces exhibited between Sn−S layers,[20] that generate substantial energy distribution and strong charge transfer resulting in electronic coupling between adjacent layers.[20,21] Low-temperature liquid metals present an opportunity to obtain ultrathin layers[22,23] with relatively large lateral dimensions. As a material that can be processed at low temperature, SnS is an excellent candidate to be synthesized in its atomically thin-form

Prof. M. J. S. Spencer
ARC Centre of Excellence in Future Low-Energy Electronics Technologies
School of Science
RMIT University
GPO Box 2476, Melbourne, Victoria 3001, Australia

Dr. S. Balendhran, Prof. K. B Crozier
School of Physics
The University of Melbourne
Melbourne, Victoria 3010, Australia

Prof. K. B Crozier
Department of Electrical and Electronic Engineering
The University of Melbourne
Melbourne, Victoria 3010, Australia

Prof. K. B Crozier
Australian Research Council (ARC) Centre of Excellence for
Transformative Meta-Optical Systems
The University of Melbourne
Melbourne, Victoria 3010, Australia

Dr. Z. Li, Prof. L. Fu
Department of Electronic Materials Engineering
Research School of Physics
The Australian National University
Canberra, ACT 2601, Australia

Prof. L. Fu
Australian Research Council (ARC) Centre of Excellence for
Transformative Meta-Optical Systems
The Australian National University
Canberra, ACT 2601, Australia

Dr. B. Shabbir
Department of Materials Science and Engineering
Monash University
Clayton, Victoria 3800, Australia

Dr. B. Shabbir
ARC Centre of Excellence in Future Low-Energy Electronics Technologies
(FLEET)
Monash University
Clayton, Victoria 3800, Australia

Prof. K. Kalantar-Zadeh
School of Chemical Engineering
University of New South Wales (UNSW)
Sydney, New South Wales 2052, Australia

using this approach and be deployed as functional layers for wide-band photodetectors that have not been reported to date.

Here, we deploy a unique synthesis technique that results in a single unit cell thick SnS layers with lateral dimensions up to the millimeter scale. The technique relies on sulfurizing the top surface of molten tin (Sn). Subsequently, we isolate Sn−S that appears at the top surface of the molten Sn using a vdW transfer technique (**Figure 1**a and Note 2, Supporting Information).[22,24] The non-polarized nature of the molten Sn results in the absence of macroscopic forces between Sn and its sulfurized skin, allowing a clean delamination. As such, the as-obtained large-area SnS layers are utilized to demonstrate ultrasensitive broadband photodetectors with more than three orders of magnitude higher responsivity ($10^2$–$10^3$ A W$^{-1}$) than commercial photodetectors and detectivity in the range ($10^9$–$10^{10}$ Jones) for wavelengths ranging from 280 to 850 nm. Considering the quest for miniaturizing devices, this work showcases a high-performance SnS photodetector with a functional layer that is sub-1 nm thick. This provides an exciting pathway toward miniaturizing light detection devices which will expand their breadth of applications.

As a substrate, we used doped silicon with a 300-nm thick layer of $SiO_2$. The as-grown SnS layers, on the surface of liquid metal Sn, were transferred onto a pre-cleaned substrate through vdW transfer technique. In Figure 1b and Note 3, Supporting Information, optical microscopy images clearly show a large lateral synthesis of SnS layers. The low magnification transmission electron microscopy (TEM) image reveals the growth of homogenous SnS layers with ultrathin features (Figure 1c). The selected area electron diffraction (SAED) pattern further reveals single crystalline features of synthesized SnS layers and their perfect orthorhombic crystal structure (inset of Figure 1c). Confirmation of single crystallinity was obtained by acquiring SAED measurements across different locations of the SnS layer (Note 4, Supporting Information). The lattice spacing of 2.8 Å correspond to the (040) plane according to the PDF#39-0354 dataset. The high-resolution TEM (HR-TEM) images show the unidirectional crystalline layers with an inter-planar distance of 2.8 Å which also corresponds to the (040) plane (Figure 1d). Figure 1e shows a representative atomic force microscopy (AFM) topological scan of as-synthesized single unit cell thick SnS layers. Here, single unit cell thick SnS layers imply two layers of SnS stacked one on top of the other and reveal a thickness of 0.8 nm (Figure 1f). The representative AFM scan of two-unit cell (that we refer to as multiple unit cell) thick layered SnS shows a thickness of ≈1.8 nm (Note 5, Supporting Information).

To further confirm the growth of monochalcogenide SnS layers, Raman spectroscopy was performed which shows active vibrational modes at 94.21, 185.61, and 219.6 cm$^{-1}$ that can be assigned to the $A_g$ phonon modes and the peak at 158.21 cm$^{-1}$ assigned to $B_{3g}$ orthorhombic mode of layered SnS (Figure 1g).[20,25] The Raman spectra obtained from the layers before and after device fabrication were identical and did not show any discernible change. The Raman peaks only show the vibrational modes associated with SnS.[18,26] Vibrational modes that can be associated with other stoichiometries and oxides are absent indicating the presence of SnS. Other characteristics such as the optical absorbance and bandgap are also in alignment with expected values for SnS.[27] EDS was performed to additionally assess the Sn and S ratios which was ≈1:1 (see Note 6, Supporting Information). A slightly

**ADVANCED**
SCIENCE NEWS

www.advancedsciencenews.com

**ADVANCED**
MATERIALS

www.advmat.de

**Figure 1.** SnS synthesis schematic and characterizations a) Schematic representation of the synthesis process. Elemental tin synthesized inside the glove box is melted on a reference substrate using a heater. The surface of the metal quickly forms a sulfide layer due to its interaction in a hydrogen sulfide ($H_2S$) environment. When a cleaned substrate is brought in contact with the molten metal, the van der Waals force between tin sulfide and the $SiO_2$ surface provides adhesion of the material onto the substrate. Delamination of the sheet becomes possible due to a weak macroscopic force that exists between the parent metal and the metal sulfide layer. b) Optical microscopy image of single unit cell thick SnS serving as the conductive channel in our photodetector. c) TEM image of SnS synthesized in a sulfide environment, using a TEM grid as the substrate. Inset of (c): SAED image of the sample indexed to SnS. d) HR-TEM image of the sample display a d-spacing of 2.8 Å matched to the (040) plane. e) AFM image of the delaminated single unit cell thick SnS layers. f) Thickness profile of the AFM image reveal a thickness of 0.8 nm. (Thickness for the AFM = $0.3 \times 2$ nm − two layers + vdW gap of 0.2 nm). g) Raman spectrum of layered SnS measured under ambient conditions along with the spectrum of the $SiO_2/Si$ substrate. h) XPS spectra of Sn−S $3d_{5/2}$ and $3d_{3/2}$ exposing peaks at 486.1 eV and 494.5 eV. i) XPS spectra of the $S2p_{3/2}$ and $S2p_{1/2}$ peaks at 161.7 eV and 162.8 eV.

ADVANCED
SCIENCE NEWS
www.advancedsciencenews.com

ADVANCED
MATERIALS
www.advmat.de

lower ratio of S than Sn which can be expected due to the interaction of atomically thin SnS with high energy X-rays.

Chemical states and stoichiometry of the synthesized SnS sample was investigated by X-ray photoelectron spectroscopy (XPS) measurements. Sn 3d and S 2p core level spectra were recorded and de-convoluted into their corresponding chemical species as shown in Figure 1h,i, respectively. The Sn 3d core level spectrum reveals a spin orbit splitting of 8.4 eV which corresponds to the Sn $3d_{3/2}$ and Sn $3d_{5/2}$ spin states. The Sn 3d core level spectrum is de-convoluted and fitted with only one contribution representing Sn−S chemical state. The peak position at 486.1 and 494.5 eV corresponds to the Sn $3d_{5/2}$ and Sn $3d_{3/2}$ spin states for Sn−S. The S 2p core level spectra were also recorded to verify it as shown in Figure 1i. The S 2p core level spectrum reveals a spin orbit splitting of 1.1 eV which corresponds to S $2p_{3/2}$ and S $2p_{1/2}$ spin states. The de-convoluted S 2p spectrum also exhibits only one chemical interaction for S 2p where peak positions at 161.7 and 162.8 eV are associated to the S $2p_{3/2}$ and S $2p_{1/2}$ of S−Sn chemical interaction. This confirms the formation of only Sn−S in the synthesized sample. The de-convoluted XPS data of SnS sample is well supported with the previous literature.[17,28,29]

The electronic band structure of monolayer, bilayer, and trilayer SnS were obtained using density functional theory (DFT) calculations (see Note 7, Supporting Information). In the context of this study, we intend to gain insights into photocurrent generation in SnS. The band structures, band transitions, and associated bandgap values of the monolayer, bilayer, and trilayer SnS structures are depicted in **Figure 2**a–c. We also experimentally measured bandgap values (Figure 2d,e). The indirect bandgap ($E_i$) values derived via Tauc plot from absorbance measurements reveal a value of 1.81 eV for a single unit cell thick layers and 1.41 eV for multiple unit cell thick (2 single unit cell thick) SnS layers as shown in Figure 2d,e, respectively. These values closely correlate with the values obtained via the DFT calculations. Simplified band structures shown in the insets of Figure 2d,e have been attained using photoelectron spectroscopy in air (PESA) and XPS valence band measurements. Obtained Fermi level values of −4.75 eV from PESA measurement and valence band value of −0.58 eV from XPS valence analysis indicate the material is p-type in nature[30] (see Note 8, Supporting Information). The hole mobility ($\approx 35$ cm$^2$ V$^{-1}$ s$^{-1}$) and p-type nature of SnS is also confirmed using Hall-effect mobility measurement and by obtaining the transfer characteristics in a back-gated
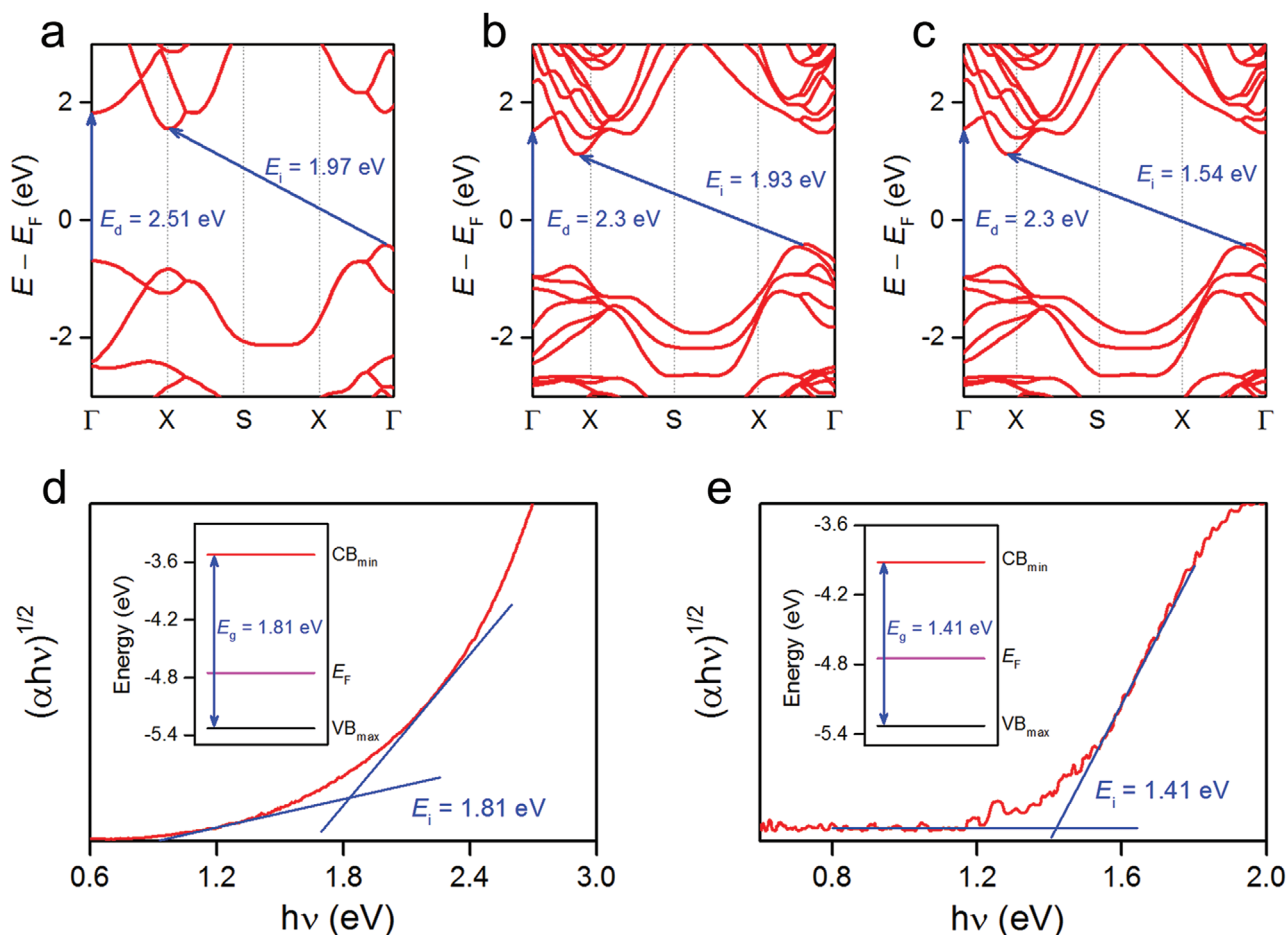


**Figure 2.** DFT calculations and experimental analysis of band structure. a) Monolayer, b) bilayer, c) trilayer SnS band structures. The arrows indicate the direct ($E_d$) and indirect ($E_i$) bandgap transitions and bandgap values in eV. The direct-bandgap values (as measured at the Gamma point) are 2.51 eV for the monolayer and 2.3 eV for the bilayers and trilayers. The indirect-bandgap values are 1.97, 1.93, and 1.54 eV for the mono-, bi-, and trilayers, respectively. d,e) Tauc plot estimating $E_i$ of the material for single and multiple unit cell SnS layers. Insets of (d) and (e) show simplified electronic band diagram indicating energy gap, Fermi level, valence, and conduction band edges of the layers of the associated thicknesses.

**ADVANCED
SCIENCE NEWS**
www.advancedsciencenews.com

**ADVANCED
MATERIALS**
www.advmat.de
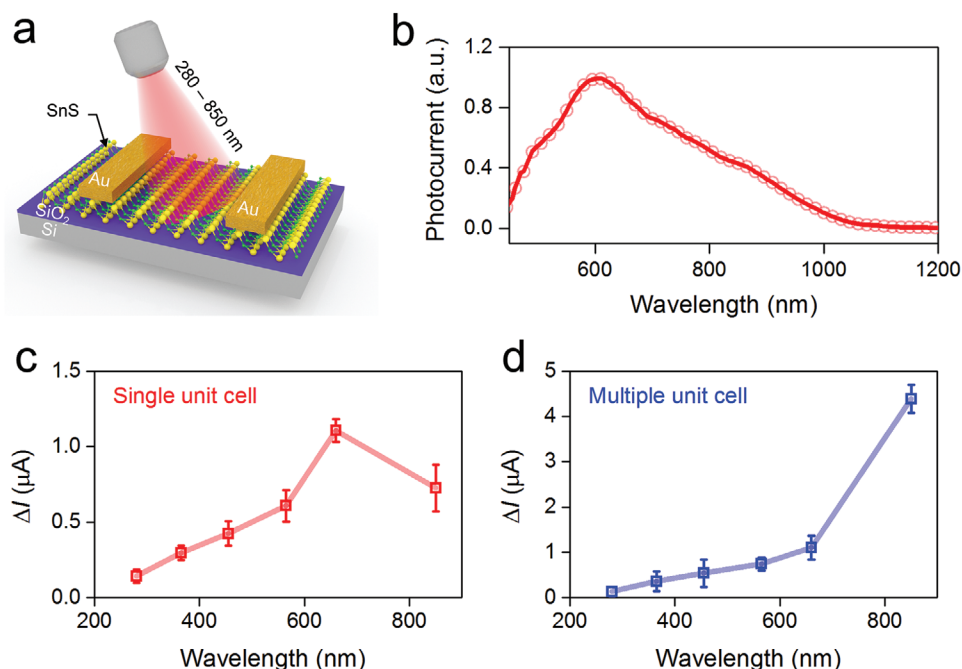
**Figure 3.** Characterization of single and multiple unit cell thick SnS layers. a) Schematic illustration of SnS photodetector fabricated on SiO$_2$/Si substrate. b) Broadband photocurrent obtained at a bias of 4.0 V and power density of 1.45 nW. c) Photocurrent measured against different wavelengths for single unit cell thick SnS layers with a maximum response at 660 nm. d) Photocurrent measured against different wavelengths for multiple-unit cell thick SnS layers with a maximum response obtained at the NIR region (850 nm) of the spectrum.

configuration (see Note 9, Supporting Information). Interestingly, Figure 2e reveals the presence of strong density of states (DOS) between 1.2 and 1.4 eV. These DOS that tend to exist within the energy bandgap of the SnS semiconductor can be associated with sulfur and/or tin vacancies in the material.[31,32] Such crystal defects lead to deep trap states that plays a significant role in the excitonic generation and recombination events that occur in a photodetector.[33]

Next, we fabricate a pair of Au electrodes with a gap of 5 µm (See **Figure 3**a and Figure S9, Note 10, Supporting Information) on separate single and multiple unit cell thick SnS layers as the semiconducting channel. The area between the electrodes is used as the active area and included in **Table 1**. To evaluate the performance of single unit cell thick SnS layers as photodetectors, room temperature photoelectrical measurements were carried out by applying a voltage bias of 4.0 V. Figure 3b shows photoresponse over a broad wavelength ranging from 400 to 1200 nm, with maximum photocurrent obtained at a wavelength of ≈620 nm. Subsequently, time-dependent photoresponse of the two-terminal devices was probed across a range of wavelengths spanning from UV (280 nm) to NIR (850 nm). The electrical response was acquired and repeated for 280 nm (UV B), 365 nm (UV A), 455 nm (blue), 565 nm (green), 660 nm (red), and 850 nm (NIR) excitations respectively. Given the large area of SnS layers resulting in uniform photocurrent generation, no specific laser alignments were required.

Devices of different thicknesses (single and multiple unit cells) were probed to observe the change in photocurrent $\Delta I$ (= $I_{illumination} - I_{dark}$) at a power density of 2.5 mW cm$^{-2}$ and a voltage bias of 2.0 V. Devices with single unit cell thick SnS layers provide a maximum response at a wavelength of 660 nm.

Here, the photoresponse behavior is attributed to its bandgap which limits the absorbed photons to an energy of 1.81 eV (681 nm) to generate photoexcited carriers. A relatively lower photoresponse is obtained beyond this regime, accompanied by a reduction in photocurrent in the NIR region. For multiple unit cell thick devices, the maximum response is obtained in the NIR region of the spectrum (850 nm) which is equivalent to the bandgap of 1.41 eV. A linearly decreasing behavior is observed in this case as the wavelength of incident light is sequentially reduced from 850 to 280 nm. To assess the repeatability of these results, photoresponse measurements were performed on more than 30 devices, for devices of both thicknesses. Photocurrents of both single unit cell and multiple unit cell thick SnS layers along with the standard deviation against each wavelength is provided in Figure 3c,d, showing the high repeatability of results. $I$–$V$ characteristics along with the photocurrent dynamics of single and multiple unit cell thick SnS devices is shown in Figure S10, Note 10, Supporting Information. We also simulate the optical properties of SnS to further understand the effect of SnS thickness and the substrate effects (Figure S11, Note 11, Supporting Information). We observe an overall increase in absorbance across the stimulated range (600–1200 nm) as SnS thickness increases and a further enhancement in the range (600–700 nm) due to the optical-cavity effect from the SiO$_2$/Si substrate.

The behavior of our SnS photodetectors can be explained in terms of absorption coefficients of relatively narrow bandgap semiconductors.[14,27] This phenomenon is induced by a reduction in photogenerated carriers available for extraction under photon flux owing to Auger processes[34] and the saturation of recombination/trap states that influence the lifetime of the generated carriers.[35] We further note that as the

**ADVANCED
SCIENCE NEWS**
www.advancedsciencenews.com

**ADVANCED
MATERIALS**
www.advmat.de

**Table 1.** Comparison of key features of our work based on SnS nanosheets with previously reported state-of-the-art photodetectors. NM: not mentioned; $P_{inc}$: illumination power density; $V$: voltage bias; $R$: responsivity; $D^*$: detectivity; EQE: external quantum efficiency; Ref: references.

| Materials | | Wavelength [nm] | Thickness [nm] | Testing conditions | | | $R$ [A W$^{-1}$] | $D^*$ [Jones] | EQE [%] | Response time [ms] | Ref. |
|---|---|---|---|---|---|---|---|---|---|---|---|
| | | | | $P_{inc}$ [mW cm$^{-2}$] | $V$ [V] | Area [μm$^2$] | | | | | |
| 2D | SnS single unit cell layers | 660 | ≈0.7 | 2.5 | 2 | 50 | $9.2 \times 10^2$ | $1.09 \times 10^9$ | $1.7 \times 10^5$ | 0.12 | This work |
| | SnS multiple unit cell layers | 850 | ≈1.8 | 2.5 | 2 | 50 | $3.51 \times 10^3$ | $6.83 \times 10^{10}$ | $1.5 \times 10^5$ | 0.16 | This work |
| | NiPS$_3$—nanosheet | 254 | 4.7 | 0.1 | 10 | 9 | $1.2 \times 10^{-1}$ | $1.2 \times 10^{12}$ | 61 | 20.7 | [66] |
| | GaSe—nanosheet | 254 | ≈4.0 | 1.0 | 5 | NM | 2.8 | NM | 1367 | 20 | [67] |
| | CdTe—nanosheet | 473 | 5–15 | 5.9 | 1 | 7 | 0.0006 | $1.0 \times 10^9$ | NM | 33.1 | [50] |
| | MoS$_2$—flakes | 633 | 10–60 | 50.0 | 1 | NM | 0.05–0.12 | $10^{10}$–$10^{11}$ | NM | NM | [68] |
| | ReS$_2$—flakes | 532 | ≈4.0 | $6.0 \times 10^{-9}$ | 4 | 2.2 | $8.8 \times 10^4$ | $1.2 \times 10^{12}$ | $2 \times 10^7$ | $>1.0 \times 10^3$ | [69] |
| | MoS$_2$—flakes | 561 | ≈0.6 | 0.024 | 8 | NM | $8.8 \times 10^2$ | NM | NM | $1.3 \times 10^4$ | [61] |
| | SnSe$_2$—flakes | 530 | ≈1.5 | 6.4 | 3 | NM | $1.1 \times 10^3$ | $1.0 \times 10^{10}$ | $2.6 \times 10^5$ | 22.6 | [70] |
| | Se:BP—flakes | 635 | 10–20 | 61.3 | 0.1 | 5–60 | 15.3 | NM | 2993 | 450 | [71] |
| | BP—flakes | 280 | 18.0 | 0.5 | 0.2 | NM | $3.6 \times 10^5$ | $2.3 \times 10^{13}$ | $1.6 \times 10^6$ | $>1.0 \times 10^3$ | [39] |
| | SnS$_2$—flakes | 532 | 1–1.6 | $1.0 \times 10^{-4}$ | NM | NM | 100 | NM | NM | $>1.0 \times 10^4$ | [49] |
| 1D | WS$_2$—crystals | 532 | 2 | $2.5 \times 10^7$ | 5 | NM | 2.5 | $9.9 \times 10^{10}$ | 583 | NM | [72] |
| | CdS—nanobelts | 490 | 200 | 3.0 | 1 | NM | $7.3 \times 10^4$ | NM | $1.9 \times 10^7$ | ≈0.02 | [73] |
| | SnS—nanobelts | 800 | 32 | 2.5 | 1 | 4.5 | $3.0 \times 10^2$ | $6 \times 10^9$ | $4.6 \times 10^4$ | 43 | [74] |
| | CdS—nanowires | 375 | NM | 0.01 | 1 | 3.21 | $2.6 \times 10^5$ | $2.3 \times 10^{16}$ | $8.6 \times 10^5$ | 192.6 | [75] |
| Thin films | ZnO:Polymer—films | 360 | ≈500 | $1.25 \times 10^{-3}$ | −9 | $5 \times 10^6$ | 721–1001 | $10^{14}$–$10^{15}$ | $(2.5–3.4) \times 10^5$ | 0.725 | [76] |
| | Graphene:$\beta$-Ga$_2$O$_3$—films | 254 | 2 | 0.3 | 2 | $8 \times 10^7$ | 1.48 | $2.2 \times 10^{12}$ | $7.3 \times 10^2$ | $3.1 \times 10^5$ | [45] |
| | SnSe—film | 370 | 9 | 0.1 | 20 | NM | 5.5 | $6 \times 10^{10}$ | $1.8 \times 10^3$ | NM | [63] |
| Commercial | Si | 400–1100 | NM | NM | 10 | $8 \times 10^5$ | 0.5 | $3 \times 10^{12}$ | NM | $1 \times 10^{-6}$ | [52] |
| | GaP | 150–550 | NM | NM | 5 | $4.8 \times 10^6$ | 0.1 | $2 \times 10^{13}$ | NM | $1.1 \times 10^{-4}$ | |
| | Ge | 800–1800 | NM | NM | 3 | $7.1 \times 10^6$ | 0.8 | $3 \times 10^{11}$ | NM | $1.2 \times 10^{-3}$ | |
| | InGaAs | 900–1700 | NM | NM | 6 | $18 \times 10^3$ | 0.9 | NM | NM | $3.5 \times 10^{-7}$ | |

illumination wavelength nears the bandgap energy of SnS, the photocurrent increases. Incident photons with an energy similar to the bandgap are efficiently absorbed with lower energy loss compared to higher energy photons resulting from lower wavelength illumination.[36] As the illumination of devices is global, temperature differences (if any) will be similar between the two interfaces of electrodes and therefore it is safe to assume negligible contribution from the photo-thermoelectric effect.[37]

**Figure 4**a,b shows photoresponse as a function of the incident power for devices with single and multiple unit cell thick SnS layers. The linear increase in photocurrent with increasing illumination power density can be associated with the photoconductive effect.[38] Responsivity ($R$) is one of the most critical figures of merit used to define the performance of a photodetector. $R$ of the photodetector is calculated from the formula[39,40]

$$R = \frac{\Delta I}{P_{inc} \times S} \quad (1)$$

where $\Delta I$ is the change in photocurrent, $P_{inc}$ the power density for a wavelength and $S$ the effective area between the electrodes of the material subjected to illumination. $R$ at an

illumination intensity of 2.5 mW cm$^{-2}$ for single unit cell thick SnS device is calculated to be 927 A W$^{-1}$ (at $\lambda = 660$ nm) and 3510 A W$^{-1}$ for multiple unit cell thick SnS device at $\lambda = 850$ nm (Figure 4c,d). Additionally, $R$ for other wavelengths is in the range $10^2$–$10^3$ A W$^{-1}$ which indicates the ultrasensitive nature of the photodetector. We plot responsivity values for various illumination intensities (see Figure S12a,b, Note 12, Supporting Information) which reveal a decreasing trend with increasing intensities.

Noise equivalent power (NEP) is also an important parameter that governs the sensitivity of the photodetector and can be expressed as[41–43]

$$NEP = \frac{i_n}{R} = \frac{(S \times \Delta f)^{1/2}}{D^*} \quad (2)$$

where $i_n$ is the noise current and $R$ is the responsivity of the device. The noise current of our single-unit cell and multiple unit cell thick SnS photodetector was measured with the help of a lock in amplifier (Figure S13, Note 13, Supporting Information). NEP values derived from noise current measurements were calculated to be $6.18 \times 10^{-13}$ W for single unit cell-thick SnS device and $3.46 \times 10^{-14}$ W for multiple unit cell thick SnS device.

**ADVANCED
SCIENCE NEWS**
www.advancedsciencenews.com

**ADVANCED
MATERIALS**
www.advmat.de
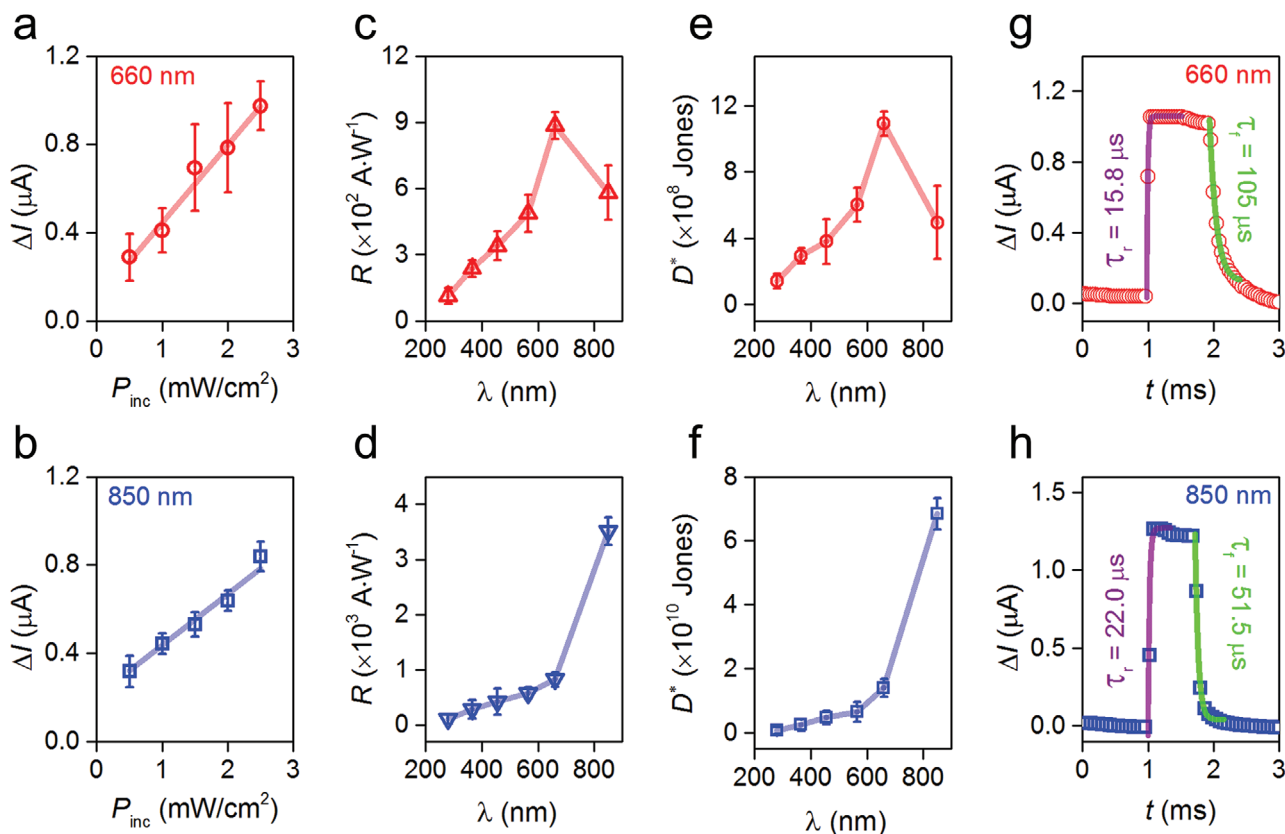
**Figure 4.** Figures of merit for single unit cell thick and multiple unit cell thick SnS layers. a,b) Photocurrent at different power intensities showing a linear dependence curve for: a) single unit cell thick SnS layers under the wavelength of 660 nm and b) multiple-unit cell thick SnS layers at 850 nm wavelength. c,d) Responsivity obtained at $P_{inc}$ = 2.5 mW cm$^{-2}$ and $V_{ds}$ = 2.0 V at different wavelengths for: c) single unit cell and d) multiple unit cell thick SnS layers. e,f) Detectivity obtained at $P_{inc}$ = 2.5 mW cm$^{-2}$ and $V_{ds}$ = 2.0 V at different wavelengths for: e) single unit cell thick and f) multiple-unit cell thick SnS layers. g) Response time of single unit cell thick SnS layers at a wavelength of 660 nm at an illumination frequency of 500 Hz. h) Response time of multiple-unit cell thick SnS layers at a wavelength of 850 nm and at a frequency of 500 Hz.

Detectivity from Equation (2) can be rearranged as[41,43,44]

$$D^* = \frac{(S \times \Delta f)^{1/2} \times R_i}{i_n} \quad (3)$$

where $R_i$ is the responsivity for a wavelength, S is the effective area subjected to illumination and $\Delta f$ is the bandwidth. The peak detectivity obtained at a power density of 2.5 mW cm$^{-2}$ for single unit cell thick SnS device is observed for $\lambda$ = 660 nm and calculated to be $1.09 \times 10^9$ cm Hz$^{1/2}$ W$^{-1}$ (Jones) whereas a peak detectivity of $6.83 \times 10^{10}$ Jones for multiple unit cell thick SnS layers is obtained at $\lambda$ = 850 nm as shown in Figure 4e,f. Furthermore, the $D^*$ for various power densities obtained by taking noise spectral density into account is plotted in Figure S12c,d, Note 12, Supporting Information, explaining the photosaturation effect of the device.

The photoconversion ability of a photodetector is defined by its external quantum efficiency (EQE) expressed as,[40,44,45]

$$EQE = \frac{h \times c \times R}{e \times \lambda} \quad (4)$$

where $h$ is the Planck's constant, $c$ is the velocity of light, $e$ is the charge of an electron, $\lambda$ is the wavelength of incident light, and $R$ is the responsivity of the photodetector. EQE value obtained here for single unit cell thick SnS layers at $\lambda$ = 660 nm

is $1.74 \times 10^5$% and $1.53 \times 10^5$% for multiple unit cell thick SnS layers at $\lambda$ = 850 nm when measured at an illumination intensity of 2.5 mW cm$^{-2}$, is shown in Figure S12e,f, Note 12, Supporting Information. EQE as a measure of voltage bias is also presented in Figure S12g,h, Note 12 Supporting Information.

The response speed at various pulsed frequencies governs the operational speed of the photodetector which is crucial in determining its viability for practical applications. For instance, the ability of a photodetector to follow optical signals of various types could pave the way for its use in NIR imaging.[46] Herein, we investigated the performance of our single unit cell and multiple unit cell thick photodetectors, for all wavelengths, which show no significant decay in the photocurrent when the frequency values varied between 0.1 and 500 Hz (see Figure S14, Note 14, Supporting Information). Furthermore, the transient response times (rise and fall times) of the photocurrent was also measured for all wavelengths at a power density of 2.5 mW cm$^{-2}$. The response time is calculated by exponentially fitting the experimental data.[47] Rise time constant ($\tau_r$) and decay time constant ($\tau_d$) is the time required for the photocurrent to reach 63% of its steady state value from its initial value and vice versa.[48] Values for $\tau_r$ and $\tau_d$ are obtained as 15.8 and 105 $\mu$s for single unit cell thick SnS layers, under the wavelength of 660 nm at 500 Hz illumination frequency (Figure 4g). Rise time ($t_r$) and decay time ($t_d$) is defined as the time required for the

**ADVANCED
SCIENCE NEWS**
www.advancedsciencenews.com

**ADVANCED
MATERIALS**
www.advmat.de

photocurrent to increase from 10% and reach 90% of its peak value and vice versa.[48,49] The rise and fall times are calculated as $t_r = \tau_r \times 2.197$ and $t_d = \tau_d \times 2.197$, respectively.[48] Hence, the rise and fall time obtained for single unit cell thick SnS layers at 660 nm are 34.71 and 230.7 μs, respectively. Similarly, for multiple unit cell thick SnS layers, $\tau_r$ and $\tau_d$ were obtained as 22 μs and 51.5 μs under the illumination wavelength of 850 nm and illumination frequency of 500 Hz (Figure 4h), which gives $t_r$ and $t_d$ values of 48.33 and 113.14 μs, respectively. It is noted that, in all cases, the rise time is faster than the decay time. A relatively slower decay time could be a result of defects present in the system, where the life time of holes is prolonged in the trapped regions of layered SnS.[49–51]

We consider the mechanism underpinning the high EQE and relatively fast response times in detail in Note 15, Supporting Information.

The gate dependent characteristics along with the figures of merit under different gate voltages is shown in Note 16, Supporting Information. Gate dependent measurements indicate that photocurrent dominates over thermionic tunneling currents across the entire operating range of gate voltages.

Existing commercially available photodetectors are typically made from silicon (Si), gallium phosphide (GaP), germanium (Ge) and indium gallium arsenide (InGaAs). The comparison of performance parameters in Table 1 show superior figures of merits. The responsivity and detectivity values of commercial photodetectors are in the range of 0.1–1 A W$^{-1}$ and $10^{11}$–$10^{13}$ Jones, respectively.[52] Nevertheless, formation of large densities of defects in the growth process of materials,[53] requirements of high processing temperature[54] and cryogenic cooling systems for efficient operation,[55] incompatibility with flexible platforms and bulkiness[53] are some of their ongoing challenges. For instance, InGaAs based photodetectors rely on complex fabrication steps particularly requiring lattice matching and surface passivation.[56,57] On the other hand, SnS depicts a self-terminating lattice while being compact and showing higher responsivities in NIR range at room temperature. Also, it is to be noted that figures of merit values of commercial photodetectors mentioned in Table 1 are recorded at a bias voltage of more than 2.0 V. So, the power consumption of the devised SnS photodetectors is relatively less in comparison to state-of-the-art photodetectors. 2D semiconductor-based photodetectors have showcased values as high as $10^0$–$10^5$ A W$^{-1}$ for responsivity, $10^9$–$10^{16}$ Jones for detectivity and $10^1$–$10^7$% for external quantum efficiency (listed in Table 1). In this work, responsivities that are three orders of magnitude higher than commercial Si photodetectors (in case of Si responsivities typically drop further at longer wavelengths) and InGaAs photodetectors are showcased. Taking material characteristics into consideration, Cadmium (Cd) is a heavy metal ion and extremely hazardous in nature,[58] degradation of BP under ambient atmosphere remains a key issue till date,[59,60] the heavy electrons in molybdenum disulphide makes it an unfavorable material for high speed photodetection applications,[61–63] tin disulphide (SnS$_2$) as another sulfide of Sn has a relatively wider bandgap restricting its detection limits up to the visible range only.[64] Sn does not suffer from such drawbacks as it is an earth abundant and relatively safe metal.[5,65] In addition, SnS provide high chemical stability[5] and air stability[5,65] rendering it a truly exceptional material for leading edge applications in optoelectronics.

In conclusion, we have successfully presented repeatable synthesis of large-area single and multiple unit cell thick SnS layers by utilizing vdW transfer of molten Sn onto conventional substrates. Experimental characterizations of the synthesized SnS layers confirm a reduction in bandgap with increasing thickness of layers which is further validated by theoretical calculations. The alluring material properties of atomically thin layered SnS have been elucidated by demonstrating broadband photodetectors operating in 280 to 850 nm wavelength range. The figures of merit obtained for our broadband photodetectors show more than three order of magnitude responsivities as compared to the state-of-the-art commercial photodetectors. The stability of atomically thin SnS layers even at such low thicknesses is a significant advantage. As such, our work proposes a new avenue for large-area synthesis of ultra-thin layers of a representative material that cannot normally be synthesized in atomically thin form using conventional processes and adapt it for high-performance optoelectronics. This also opens pathways toward discovering the unique properties that could exist at the quantum limit of other layered materials.

## Experimental Section

*Material Synthesis and Fabrication*: Experiments were conducted in a controlled environment in a specially designed glove box. Initially, a continuous supply of nitrogen at a flow rate 0.5 sccm was maintained for about 4 h to ensure complete removal of oxygen. After which, H$_2$S gas was introduced at a flow rate of 0.5 sccm for 1 h to attain a homogeneous sulfide rich atmosphere within the glove box. Elemental tin was molten with the aid of a ceramic heater at a temperature of 350 °C by applying a voltage of 12 V using a power supply unit. The initial thick layer from the surface of molten metal was removed through pre-conditioning prior to transferring freshly grown nanosheets onto desired substrates (SiO$_2$, Si, glass, TEM grids, etc.). The freshly formed liquid metal undergoes a color change from silver to dull yellow within a few seconds confirming the formation of the metal sulfide layer on the surface of metal-melt. Prior to touch printing, substrates were placed on the heater to avoid thermal shock. When TEM grids were utilized for transferring the material, the grids were placed on PDMS to avoid breakage of the fragile grids. Standard photolithography was used to pattern electrodes. Metal Cr (10 nm)/Au (100 nm) was deposited on the developed patterns using electron beam evaporation technique at a pressure less than $3 \times 10^{-7}$ mbar. Lift-off was done in acetone to reveal the required metal contacts.

*Structural Characterizations*: AFM measurement was conducted using the Bruker Dimension Icon AFM in ScanAsyst mode. Raman spectra were obtained on SnS/SiO$_2$/Si samples using the Horiba Scientific Raman spectrometer utilizing 532 nm laser source operating at 9 mW excitation power, 50× objective, and 1800 grating. XPS was carried out using a Thermo K-Alpha instrument equipped with a monochromatic Al K$\alpha$ source (photon energy of 1486.7 eV and pressure of $1 \times 10^9$ mbar). UV–vis absorbance measurements were collected using a CRAIC 20/30 microspectrophotometer. The obtained binding energy was calibrated using C 1s peak at 284.8 eV.

Low-magnification TEM and HR-TEM were conducted using JEOL 1010 and 2100F microscopes. The JEOL 1010 was equipped with a Gatan Orius SC600A CCD camera and operated at an accelerating voltage of 100 keV. JEOL 2100F microscope was equipped with a Gatan Orius SC1000 CCD camera. This instrument has an accelerating voltage of 80 keV.

*Electrical and Optoelectronic Measurements*: Electrical measurements were carried out using the B2901A source meter and FET measurements were carried out using the Keithley 4200SCS semiconductor parameter analyzer. For the optoelectronic measurements, commercial monochromatic light emitting diodes (Thorlabs, Inc.) with different wavelengths ranging from 280 to 850 nm were used as excitation sources.

All measurements were performed in the dark and ambient light with exposure to only the target illumination wavelengths. The illumination power was calibrated by a commercial UV-enhanced photodetector (Newport Corporation). The laser beam was directed onto the nanosheets vertically at a fixed distance of about 1.7 cm from the sample holder. Electrical characterizations for various light sources were repeated under different illumination intensities in the range of 0.5 to 2.5 mW cm$^{-2}$. The shape of the beam of light was Gaussian in nature. The frequency and pulse width modulation of the light sources were performed by using the Arduino-Uno programmable microcontroller board.

The photocurrent was detected using a lock-in detection system including an Agilent 33210A 10 MHz function/arbitrary waveform generator, a Stanford SR570 low-noise current pre-amplifier and a Stanford SR850 digital lock-in amplifier. (The reflected light was measured simultaneously using a confocal microscope and a Si avalanche photodiode detector). The generator frequency was 333 Hz and the applied voltage was 4 V.

## Supporting Information

Supporting Information is available from the Wiley Online Library or from the author.

## Conflict of Interest

The authors declare no conflict of interest.

[1] Z. Tian, C. Guo, M. Zhao, R. Li, J. Xue, *ACS Nano* **2017**, *11*, 2219.
[2] H. Wang, X. Qian, *2D Mater.* **2017**, *4*, 015042.
[3] P. Z. Hanakata, A. Carvalho, D. K. Campbell, H. S. Park, *J. Phys. Rev. B* **2016**, *94*, 035304.
[4] L. C. Gomes, A. Carvalho, A. H. Castro Neto, *J. Phys. Rev. B* **2016**, *94*, 054103.
[5] Z. Hu, Y. Ding, X. Hu, W. Zhou, X. Yu, S. Zhang, *Nanotechnology* **2019**, *30*, 252001.
[6] J. R. Brent, D. J. Lewis, T. Lorenz, E. A. Lewis, N. Savjani, S. J. Haigh, G. Seifert, B. Derby, P. O'brien, *J. Am. Chem. Soc.* **2015**, *137*, 12689.
[7] C. Xin, J. Zheng, Y. Su, S. Li, B. Zhang, Y. Feng, F. Pan, *J. Phys. Chem. C* **2016**, *120*, 22663.
[8] M. Patel, A. Chavda, I. Mukhopadhyay, J. Kim, A. Ray, *Nanoscale* **2016**, *8*, 2293.
[9] Q. Zhang, X. Chen, W.-C. Liu, Y. Wang, *Comput. Mater. Sci.* **2019**, *158*, 272.
[10] A. Arash, T. Ahmed, A. Govind Rajan, S. Walia, F. Rahman, A. Mazumder, R. Ramanathan, S. Sriram, M. Bhaskaran, E. Mayes, M. S. Strano, S. Balendhran, *2D Mater.* **2019**, *6*, 035031.
[11] G. H. Yue, D. L. Peng, P. X. Yan, L. S. Wang, W. Wang, X. H. Luo, *J. Alloys Compd.* **2009**, *468*, 254.
[12] L. Pan, S. Yuan, J. Lin, B. Zou, L.-J. Shi, *J. Phys.: Condens. Matter* **2018**, *30*, 465302.
[13] Z. Deng, D. Cao, J. He, S. Lin, S. M. Lindsay, Y. Liu, *ACS Nano* **2012**, *6*, 6197.
[14] K. T. Ramakrishna Reddy, N. Koteswara Reddy, R. W. Miles, *Sol. Energy Mater. Sol. Cells* **2006**, *90*, 3041.
[15] S. Sucharitakul, U. Rajesh Kumar, R. Sankar, F.-C. Chou, Y.-T. Chen, C. Wang, C. He, R. He, X. P. A. Gao, *Nanoscale* **2016**, *8*, 19050.
[16] L. Makinistian, E. A. Albanesi, *Basic Solid State Phys.* **2009**, *246*, 183.
[17] L. S. Price, I. P. Parkin, A. M. E. Hardy, R. J. H. Clark, T. G. Hibbert, K. C. Molloy, *Chem. Mater.* **1999**, *11*, 1792.
[18] P. Sinsermsuksakul, J. Heo, W. Noh, A. S. Hock, R. G. Gordon, *Adv. Energy Mater.* **2011**, *1*, 1116.
[19] L. A. Burton, D. Colombara, R. D. Abellon, F. C. Grozema, L. M. Peter, T. J. Savenije, G. Dennler, A. Walsh, *Chem. Mater.* **2013**, *25*, 4908.
[20] N. Higashitarumizu, H. Kawamoto, M. Nakamura, K. Shimamura, N. Ohashi, K. Ueno, K. Nagashio, *Nanoscale* **2018**, *10*, 22474.
[21] H.-Y. Song, J.-T. Lü, *Chem. Phys. Lett.* **2018**, *695*, 200.
[22] A. Zavabeti, J. Z. Ou, B. J. Carey, N. Syed, R. Orrell-Trigg, E. L. H. Mayes, C. Xu, O. Kavehei, A. P. O'Mullane, R. B. Kaner, K. Kalantar-Zadeh, T. Daeneke, *Science* **2017**, *358*, 332.
[23] B. J. Carey, J. Kaur, M. Wuest, F. Wuest, *Nat. Commun.* **2017**, *8*, 1.
[24] T. Daeneke, P. Atkin, R. Orrell-Trigg, A. Zavabeti, T. Ahmed, S. Walia, M. Liu, Y. Tachibana, M. Javaid, A. D. Greentree, S. P. Russo, R. B. Kaner, K. Kalantar-Zadeh, *ACS Nano* **2017**, *11*, 10974.
[25] J. Xia, X.-Z. Li, X. Huang, N. Mao, D.-D. Zhu, L. Wang, H. Xu, X.-M. Meng, *Nanoscale* **2016**, *8*, 2063.
[26] M. Li, Y. Wu, T. Li, Y. Chen, H. Ding, Y. Lin, N. Pan, X. Wang, *RSC Adv.* **2017**, *7*, 48759.
[27] A. P. Lambros, D. Geraleas, N. A. Economou, *J. Phys. Chem. Solids* **1974**, *35*, 537.
[28] A. Rauf, M. S. Arif Sher Shah, J. Y. Lee, C.-H. Chung, J. W. Bae, P. J. Yoo, *RSC Adv.* **2017**, *7*, 30533.
[29] G. Matyszczak, A. Fidler, E. Polesiak, M. Sobieska, K. Morawiec, W. Zajkowska, K. Lawniczak-Jablonska, P. Kuzmiuk, *Ultrason. Sonochem.* **2020**, *68*, 105186.
[30] E. Guneri, F. Gode, C. Ulutas, F. Kirmizigul, G. Altindemir, C. Gumus, *Chalcogenide Lett.* **2010**, *7*, 685.
[31] J. Vidal, S. Lany, M. D'avezac, A. Zunger, A. Zakutayev, J. Francis, J. Tate, *Appl. Phys. Lett.* **2012**, *100*, 032104.
[32] R. S. Datta, J. Z. Ou, M. Mohiuddin, B. J. Carey, B. Y. Zhang, H. Khan, N. Syed, A. Zavabeti, F. Haque, T. Daeneke, K. Kalantar-Zadeh, *Nano Energy* **2018**, *49*, 237.
[33] T. Leijtens, G. E. Eperon, A. J. Barker, G. Grancini, W. Zhang, J. M. Ball, A. R. S. Kandada, H. J. Snaith, A. Petrozza, *Energy Environ. Sci.* **2016**, *9*, 3472.
[34] A. M. White, *J. Cryst. Growth* **1988**, *86*, 840.

[35] Y. Fang, Q. Dong, Y. Shao, Y. Yuan, J. Huang, *Nat. Photonics* **2015**, *9*, 679.

[36] S. Hwan Lee, D. Lee, W. Sik Hwang, E. Hwang, D. Jena, W. Jong Yoo, *Appl. Phys. Lett.* **2014**, *104*, 193113.

[37] N. Perea-López, Z. Lin, N. R. Pradhan, A. Iñiguez-Rábago, A. Laura Elías, A. Mccreary, J. Lou, P. M. Ajayan, H. Terrones, L. Balicas, M. Terrones, *2D Mater.* **2014**, *1*, 011004.

[38] E. H. Putley, *Appl. Opt.* **1965**, *4*, 649.

[39] T. Ahmed, S. Kuriakose, S. Abbas, M. J. S. Spencer, M. A. Rahman, M. Tahir, Y. Lu, P. Sonar, V. Bansal, M. Bhaskaran, S. Sriram, S. Walia, *Adv. Funct. Mater.* **2019**, *29*, 1901991.

[40] S. Chen, C. Teng, M. Zhang, Y. Li, D. Xie, G. Shi, *Adv. Mater.* **2016**, *28*, 5969.

[41] C. Xie, P. You, Z. Liu, L. Li, F. Yan, *Light: Sci. Appl.* **2017**, *6*, e17023.

[42] L. Dou, Y. (M.) Yang, J. You, Z. Hong, W.-H. Chang, G. Li, Y. Yang, *Nat. Commun.* **2014**, *5*, 5404.

[43] C. Xie, C. K. Liu, H. L. Loi, F. Yan, *Adv. Funct. Mater.* **2020**, *30*, 1903907.

[44] C. Xie, C. Mak, X. Tao, F. Yan, *Adv. Funct. Mater.* **2017**, *27*, 1603886.

[45] W.-Y. Kong, G.-A. Wu, K.-Y. Wang, T.-F. Zhang, Y.-F. Zou, D.-D. Wang, L.-B. Luo, *Adv. Mater.* **2016**, *28*, 10725.

[46] X. Gong, M. Tong, Y. Xia, W. Cai, J. S. Moon, Y. Cao, G. Yu, C.-L. Shieh, B. Nilsson, A. J. Heeger, *Science* **2009**, *325*, 1665.

[47] A. Gundimeda, S. Krishna, N. Aggarwal, A. Sharma, N. D. Sharma, K. K. Maurya, S. Husale, G. Gupta, *Appl. Phys. Lett.* **2017**, *110*, 103507.

[48] S. K. Jain, N. Aggarwal, S. Krishna, R. Kumar, S. Husale, V. Gupta, G. Gupta, *J. Mater. Sci.: Mater. Electron.* **2018**, *29*, 8958.

[49] Y. Huang, E. Sutter, J. T. Sadowski, M. Cotlet, O. L. A. Monti, D. A. Racke, M. R. Neupane, D. Wickramaratne, R. K. Lake, B. A. Parkinson, P. Sutter, *ACS Nano* **2014**, *8*, 10743.

[50] R. Cheng, Y. Wen, L. Yin, F. Wang, F. Wang, K. Liu, T. A. Shifa, J. Li, C. Jiang, Z. Wang, J. He, *Adv. Mater.* **2017**, *29*, 1703122.

[51] T. Ahmed, S. Kuriakose, E. L. H. Mayes, R. Ramanathan, V. Bansal, M. Bhaskaran, S. Sriram, S. Walia, *Small* **2019**, *15*, 1900966.

[52] Thorlabs Inc., https://www.thorlabs.com/newgrouppage9.cfm?-objectgroup_id=285 (accessed: August 2020).

[53] R. Saran, R. J. Curry, *Nat. Photonics* **2016**, *10*, 81.

[54] G. Konstantatos, E. H. Sargent, *Proc. IEEE* **2009**, *97*, 1666.

[55] P. Martyniuk, A. Rogalski, *Opto-Electron. Rev.* **2013**, *21*, 239.

[56] T. Yagi, Y. Fujiwara, T. Nishino, Y. Hamakawa, *Jpn. J. Appl. Phys.* **1983**, *22*, L467.

[57] I. Kimukin, N. Biyikli, B. Butun, O. Aytur, S. M. Unlu, E. Ozbay, *IEEE Photonics Technol. Lett.* **2002**, *14*, 366.

[58] A.-R. Hong, J. Kim, S. Y. Kim, S.-I. Kim, K. Lee, H. S. Jang, *Opt. Lett.* **2015**, *40*, 4959.

[59] T. Ahmed, S. Balendhran, M. N. Karim, E. L. H. Mayes, M. R. Field, R. Ramanathan, M. Singh, V. Bansal, S. Sriram, M. Bhaskaran, S. Walia, *npj 2D Mater. Appl.* **2017**, *1*, 18.

[60] J. D. Wood, S. A. Wells, D. Jariwala, K.-S. Chen, E. Cho, V. K. Sangwan, X. Liu, L. J. Lauhon, T. J. Marks, M. C. Hersam, *Nano Lett.* **2014**, *14*, 6964.

[61] O. Lopez-Sanchez, D. Lembke, M. Kayci, A. Radenovic, A. Kis, *Nat. Nanotechnol.* **2013**, *8*, 497.

[62] A. Di Bartolomeo, L. Genovese, T. Foller, F. Giubileo, G. Luongo, L. Croin, S.-J. Liang, L. K. Ang, M. Schleberger, *Nanotechnology* **2017**, *28*, 214002.

[63] J. Yao, Z. Zheng, G. Yang, *Adv. Funct. Mater.* **2017**, *27*, 1701823.

[64] X. Zhou, Q. Zhang, L. Gan, H. Li, T. Zhai, *Adv. Funct. Mater.* **2016**, *26*, 4405.

[65] N. Koteeswara Reddy, M. Devika, E. S. R. Gopal, *Crit. Rev. Solid State Mater. Sci.* **2015**, *40*, 359.

[66] J. Chu, F. Wang, L. Yin, L. Lei, C. Yan, F. Wang, Y. Wen, Z. Wang, C. Jiang, L. Feng, J. Xiong, Y. Li, J. He, *Adv. Funct. Mater.* **2017**, *27*, 1701342.

[67] P. Hu, Z. Wen, L. Wang, P. Tan, K. Xiao, *ACS Nano* **2012**, *6*, 5988.

[68] W. Choi, M. Y. Cho, A. Konar, J. H. Lee, G.-B. Cha, S. C. Hong, S. Kim, J. Kim, D. Jena, J. Joo, S. Kim, *Adv. Mater.* **2012**, *24*, 5832.

[69] E. Liu, M. Long, J. Zeng, W. Luo, Y. Wang, Y. Pan, W. Zhou, B. Wang, W. Hu, Z. Ni, Y. You, X. Zhang, S. Qin, Y. Shi, K. Watanabe, T. Taniguchi, H. Yuan, H. Y. Hwang, Y. Cui, F. Miao, D. Xing, *Adv. Funct. Mater.* **2016**, *26*, 1938.

[70] X. Zhou, L. Gan, W. Tian, Q. Zhang, S. Jin, H. Li, Y. Bando, D. Golberg, T. Zhai, *Adv. Mater.* **2015**, *27*, 8035.

[71] Y. Xu, J. Yuan, L. Fei, X. Wang, Q. Bao, Y. Wang, K. Zhang, Y. Zhang, *Small* **2016**, *12*, 5000.

[72] H. Tan, Y. Fan, Y. Zhou, Q. Chen, W. Xu, J. H. Warner, *ACS Nano* **2016**, *10*, 7866.

[73] L. Li, P. Wu, X. Fang, T. Zhai, L. Dai, M. Liao, Y. Koide, H. Wang, Y. Bando, D. Golberg, *Adv. Mater.* **2010**, *22*, 3161.

[74] X. Zhou, L. Gan, Q. Zhang, X. Xiong, H. Li, Z. Zhong, J. Han, T. Zhai, *J. Mater. Chem. C* **2016**, *4*, 2111.

[75] D. Zheng, H. Fang, P. Wang, W. Luo, F. Gong, J. C. Ho, X. Chen, W. Lu, L. Liao, J. Wang, W. Hu, *Adv. Funct. Mater.* **2016**, *26*, 7690.

[76] F. Guo, B. Yang, Y. Yuan, Z. Xiao, Q. Dong, Y. Bi, J. Huang, *Nat. Nanotechnol.* **2012**, *7*, 798.